The Astrophysical Journal Letters, 933:L6 (11pp), 2022 July 1 https://doi.org/10.3847/2041-8213/ac786f

Faraday Conversion in Pair-symmetric Winds of Magnetars and Fast Radio Bursts

Maxim Lyutikov
Department of Physics and Astronomy, Purdue University, 525 Northwestern Avenue, West Lafayette, IN, USA; lyutikov@purdue.edu
Received 2021 November 3; revised 2022 June 11; accepted 2022 June 13; published 2022 June 29

Abstract

We consider the propagation of polarization in the inner parts of pair-symmetric magnetar winds, close to the light cylinder. Pair plasmas in magnetic field is birefringent, a $\propto B^2$ effect. As a result, such plasmas work as phase retarders: Stokes parameters follow a circular trajectory on the Poincare sphere. In the highly magnetized regime, $\omega,\ \omega_p \ll \omega_B$, the corresponding rotation rates are independent of the magnetic field. A plasma screen with dispersion measure DM $\sim 10^{-6}$ pc cm^{-3} can induce large polarization changes, including large effective rotation measures (RMs). The frequency scaling of the (generalized) RM, $\propto \lambda^{\alpha}$, mimics the conventional RM with $\alpha = 2$ for small phase shifts, but can be as small as $\alpha = 1$. In interpreting observations, the frequency scaling of polarization parameters should be fitted independently. The model offers explanations for (i) the large circular polarization component observed in FRBs, with right–left switching; (ii) large RM, with possible sign changes (when the observation bandwidth is small); and (iii) time-dependent variable polarization. A relatively dense and slow wind is needed—the corresponding effect in regular pulsars is small.

Unified Astronomy Thesaurus concepts: Radio pulsars (1353); Radio transient sources (2008); Plasma astrophysics (1261); Magnetars (992)

1. Polarization of FRBs: the Challenges

Polarization properties of FRBs defy simple classification (Caleb et al. 2019; Petroff et al. 2019: "some FRBs appear to be completely unpolarized, some show only circular polarization, some show only linear polarization, and some show both"). Understanding polarization behavior is the key to understanding FRBs.

Even in the subset of linearly polarized FRBs, there is no clear trend:

1. FRB 150807 (Ravi et al. 2016) was nearly 80% linearly polarized, but has a very small RM = 12 at DM = 266 (in usual astronomical units); the average inferred magnetic field $\langle B\rangle = 5\times 10^{-8}$ G.
2. FRB 110523 (Masui et al. 2015), RM = 186, DM = 623, $\langle B\rangle = 5\times 10^{-7}$ G
3. FRB 180301 (Price et al. 2019), RM $= 3\times 10^3$, DM = 522, $\langle B\rangle = 6\times 10^{-6}$ G.
4. FRB 121102 (Michilli et al. 2018) was 100% linearly polarized, (varying!) RM $= 10^5$, DM = 559, $\langle B\rangle = 2\times 10^{-4}$ G. At the observed frequency of ∼4.5 GHz, this corresponds to a PA rotation of 360 rad; this is a model-independent quantity to be explained (in a sense that a value of RM assumes a particular frequency scaling of the rotation of polarization).
5. The case of FRB 20190520B (Dai et al. 2022) is particularly interesting: It shows large fluctuations of linear polarization (from ∼15% to ∼60%), large fluctuations of circular polarization with changing sign (∼±10%), and large fluctuations of RM, also with changing sign ($\pm 10^4$).
6. No correspondingly large changes of DM are seen.

We make the following conclusion: The polarization model should explain not the average properties but the extremes of the behavior. Models should account for large variations in polarization properties, both between different sources, temporal variations in a given source, and unusual polarization behavior as in FRB 180301 and FRB 20190520B.

The fast temporal variation of RM seen in FRB 121102 (Michilli et al. 2018) and FRB 20190520B (Dai et al. 2022) is especially demanding, as this implies that the RM comes from a relatively compact region. This would normally require a small and extremely dense region, yet no DM variations are seen. (In our model, the region is small but not dense.)

In this paper we consider polarization propagation effects in the near wind zone of the central magnetar, somewhat outside the light cylinder. We demonstrate that the model naturally explains a broad range of polarization behaviors. The switching of the signs of circular polarization and of the (generalized) RM is especially noteworthy. We also mention related papers by Vedantham & Ravi (2019) and Gruzinov & Levin (2019) (in passing, we note a minor error: Their parameters h and g should be interchanged).

Previously a number of works considered the PA rotation effect inside the pulsar magnetosphere (Cheng & Ruderman 1979; Barnard 1986; Petrova & Lyubarskii 2000; Wang et al. 2010; Beskin & Philippov 2012). Inside the pulsar magnetosphere, the PA rotation and the generation of the V component are suppressed by a combination of effects: (i) for parallel propagation in symmetric pair plasma, the Faraday effect is absent; the contribution to the PA rotation comes either from a slight charge imbalance, different Lorentz factors, or from oblique propagation (Kazbegi et al. 1991a; Lyutikov 1999)—all of these effects produce weak contribution (due to small "active" density and/or small angle of propagation). Relativistic motion of plasma also reduces the effective plasma-frame density, and the effect of stretching of the corresponding timescale in the lab frame is also important in the present model. In contrast to the magnetospheres, in the

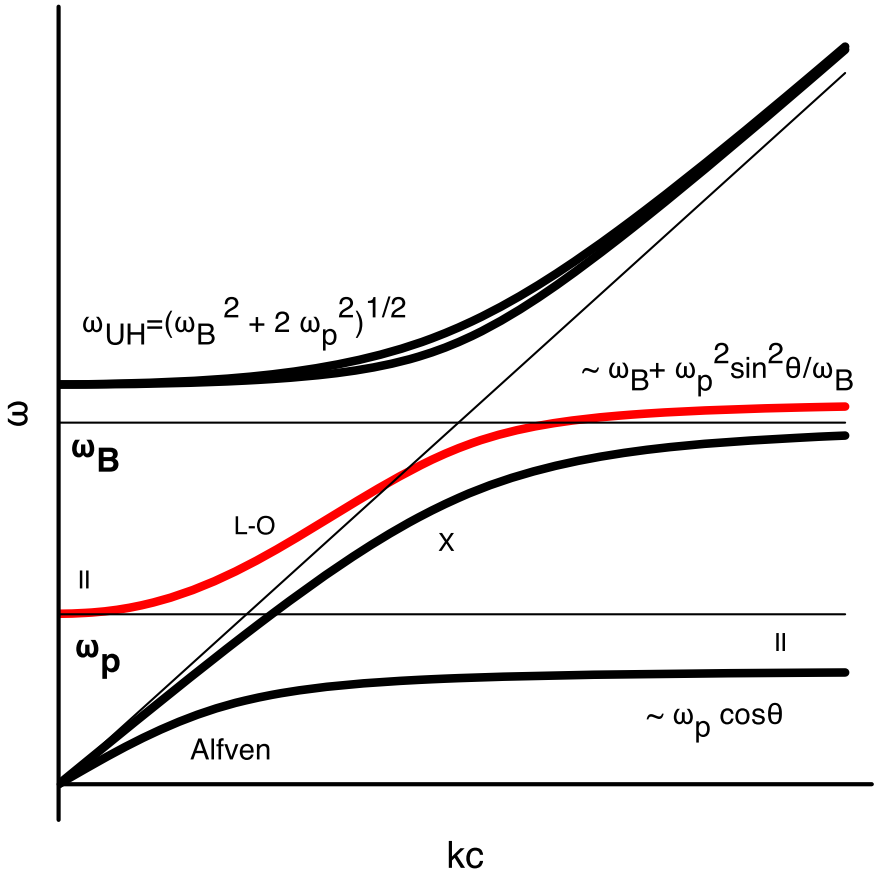

Figure 1. Wave dispersions $\omega(k)$ in pair plasma in a strong magnetic field, $\omega_B \gg \omega_p$, for oblique propagation. At low frequencies $\omega \ll \omega_B$ there are three modes labeled X (polarized orthogonally to the ***k*–*B*** plane), Alfvén, and O (both polarized in the ***k*–*B*** plane). The O mode has a resonance at $\sim\omega_B + \omega_p^2 \sin^2\theta/\omega_B$ and cutoff at $\sqrt{2}\,\omega_p$. The Alfvén mode has a resonance at $\sim\sqrt{2}\,\omega_p \cos\theta$. The sign $\|$ indicates locations where corresponding waves are nearly longitudinally polarized. The two high-frequency, $\omega > \omega_B$, waves with nearly identical dispersions have a cutoff at the upper hybrid frequency $\omega_{UH} = \sqrt{\omega_B^2 + 2\omega_p^2}$ (Lyutikov 2007).

near wind zone, it is the total plasma density that contributes to the PA rotation via the effects of birefringence.

2. Polarization Propagation in Birefringent Symmetric Pair Plasma

2.1. Faraday and Cotton-Mouton/Voigt Effects

Two somewhat different effects contribute to the changes in polarization as the light propagates in plasma: the Faraday effect and the Cotton-Mouton/Voigt effects (Landau & Lifshitz 1960). Qualitatively, the Faraday effect allows a linearly polarized wave propagating along the magnetic field to be decomposed into two circularly polarized waves. In an electron–ion plasma, the two circularly polarized waves have different phase velocities—their final addition leads to the rotation of the position angle (PA). The rate of rotation of the PA due to the Faraday effect is (Ginzburg & Syrovatskii 1965, Equation (4.6)) is

$$\frac{d\chi_F}{dl} = \frac{1}{2}\frac{\omega}{c}(\Delta n)_c, \tag{1}$$

where $(\Delta n)_c$ is the difference in the refractive index of two circularly polarized normal modes. This effect is linear in the magnetic field. It disappears in symmetric pair plasma.

The Cotton-Mouton/Voigt effects appear because for oblique propagation (with respect to the magnetic field), the two plasma modes, usually called O (ordinary) and X (extraordinary), have different phase velocities. If the initial wave had contribution from both X and O modes, the final addition of the retarded waves leads to elliptical polarization, hence both to the rotation of the position angle of the linearly polarized component and to the appearance of circular polarization. This effect is quadratic in the magnetic field—it appears both in symmetric and nonsymmetric plasmas.

Following tradition, we call the polarization transformation Faraday Conversion (FC), with a clear understanding of the different origins of the circular component, as discussed above.

2.2. Waves in Symmetric Pair Plasma

Waves in pair plasma have been considered in a number of publications (Arons & Barnard 1986; Kazbegi et al. 1991b; Lyutikov 1999); we follow Lyutikov (2007). Let us consider the simplest case of cold plasma, in the plasma frame. For an $e^{\pm}$ plasma in a magnetic field, the dispersion relation factorizes, giving two modes: the X mode with the electric vector perpendicular to the ***k*–*B*** plane and two branches of the longitudinal-transverse mode, which we will call the O and Alfvén waves, with the electric vector in the ***k*–*B*** plane (Arons & Barnard 1986; see Figure 1). X waves are a subluminal (for $\omega < \omega_B$) transverse electromagnetic wave with a dispersion

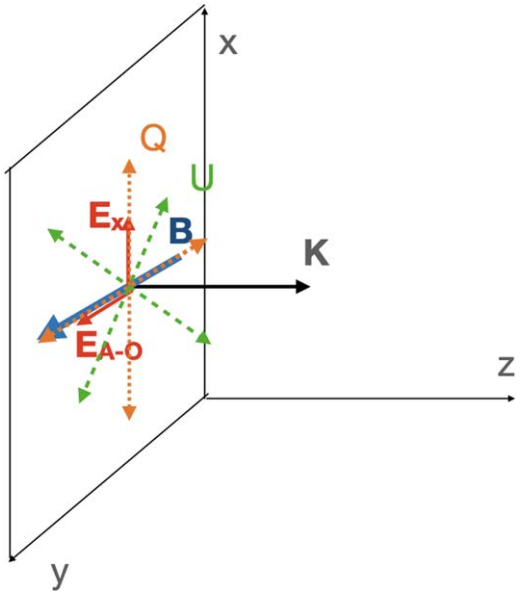

Figure 2. Coordinates, normal modes, and Stokes parameters. The wave propagates along the z direction, the magnetic field is along the y direction, the X mode is polarized along x, the A-O mode is polarized along y, Stokes Q corresponds to the pure oscillation of the electric field either along x or y (the $+$), and Stokes U corresponds to pure oscillation along the x axes. In such coordinates the Stokes Q represents a normal mode, hence there is no Faraday conversion. Stokes U is a mix of two normal modes with different phase velocities.

relation

$$n_X^2 = 1 - \frac{2\omega_p^2}{\omega^2 - \omega_B^2}, \tag{2}$$

here $n = kc/\omega$ is the refractive index, $\omega_B = eB/mc$ is the cyclotron frequency, and $\omega_p = \sqrt{4\pi n_\pm e^2/m}$ is the plasma frequency of each species (so that for a pair plasma, the total plasma frequency is $\sqrt{2}\,\omega_p$). The Alfvén O mode satisfies the dispersion relation

$$n_{A-O}^2 = \frac{(\omega^2 - 2\omega_p^2)(\omega^2 - 2\omega_p^2 - \omega_B^2)}{(\omega^2 - 2\omega_p^2)(\omega^2 - \omega_B^2) - 2\omega_B^2\omega_p^2\sin^2\theta}. \tag{3}$$

The Alfvén branch is always subluminal, while the O mode is superluminal at small wavevectors and subluminal at large wavevectors.

In the limit $\omega_p \ll \omega$, we find

$$(\Delta n) = n_X - n_{A-O} = -\frac{\omega_B^2\omega_p^2}{\omega^2(\omega^2 - \omega_B^2)}\sin^2\theta$$
$$= \begin{cases} -\frac{\omega_B^2\omega_p^2}{\omega^4}\sin^2\theta, & \omega_B \ll \omega \\ \frac{\omega_p^2}{\omega^2}\sin^2\theta, & \omega_B \gg \omega, \end{cases} \tag{4}$$

$\omega_B \ll \omega$ has been discussed previously (Sazonov 1969; Melrose 1997; Kennett & Melrose 1998). $\omega_B \gg \omega$ is the new regime of interest: In highly magnetized plasma, the phase velocity difference is independent of the magnetic field (the X mode is nearly luminal).

2.3. Faraday Conversion in Magnetized Pair Plasma

Consider the propagation of electromagnetic radiation along the z direction perpendicular to the magnetic field, which is in the y direction, Figure 2

The X mode is then polarized along x and the A-O mode along y. At the point $z = 0$ let the wave be linearly polarized with the unit Jones (Born & Wolf 1980) vector:

$$\boldsymbol{E}_0 = \begin{pmatrix} \cos\chi_0 \\ \sin\chi_0 \end{pmatrix}. \tag{5}$$

The medium works as a retarder. The key parameter is a phase lag (retardance) δ:

$$\frac{d\delta}{dz} = \frac{\omega}{c}(\Delta n). \tag{6}$$

In the limit $\omega_B \gg \omega_p,\ \omega$,

$$\frac{d\delta}{dz} = \frac{\omega_p^2}{\omega c} = \frac{2e^2 n}{c^2 m_e} \times \lambda = \delta_0 \times \lambda$$
$$\delta_0 = \frac{2e^2 n}{c^2 m_e}$$
$$\delta = \int \frac{d\delta}{dz} dz = k\int (\Delta n)$$
$$dz = \lambda\frac{2e^2}{m_e c^2} n\Delta z = 2r_e\lambda(n\Delta z) = 1.7 \times 10^6 \lambda \times \mathrm{DM}, \tag{7}$$

where (Δn) is the difference between the refractive indices of the two linearly polarized modes, with $\theta = \pi/2$ assumed; the limit "$\rightarrow$" here and below corresponds to the relevant case of $\omega_B \gg \omega$; the units of δ_0 is cm^{-2}. In the last relation, λ is in centimeters and DM is the dispersion measure in pc cm^{-3}.

It may be convenient to define the magnetic conversion measure ($\mathrm{CM_B}$) as

$$\delta = \mathrm{CM_B} \times \lambda,\ \omega_B \gg \omega$$
$$\mathrm{CM_B} = \frac{2e^2}{m_e c^2} n\Delta z = 1.7 \times 10^6 \times \mathrm{DM\ cm^{-1}}$$
$$= 1.7 \times 10^4 \times \mathrm{DM\ m^{-1}}. \tag{8}$$

It is different from the low magnetic field CM:

$$\delta = \mathrm{CM} \times \lambda^3,\ \omega_B \ll \omega$$
$$\mathrm{CM} = \frac{e^4}{2\pi^2 m_e^3 c^6} n\Delta z B^2 = 1.4 \times 10^{-2} \times \mathrm{DM} \times B^2\ \mathrm{cm^{-3}}$$
$$= 1.4 \times 10^{-8} \times \mathrm{DM} \times B^2\ \mathrm{m^{-3}}, \tag{9}$$

where the magnetic field is in Gauss.

Relations (7)–(8) demonstrate that in magnetically dominated plasma, a screen with $\mathrm{DM} \sim 10^{-6}$ pc cm^{-3} can induce polarization changes (rotation of PA of the linear component, as well as the production of a circular component) of the order of unity. This is one of the major points of this work.

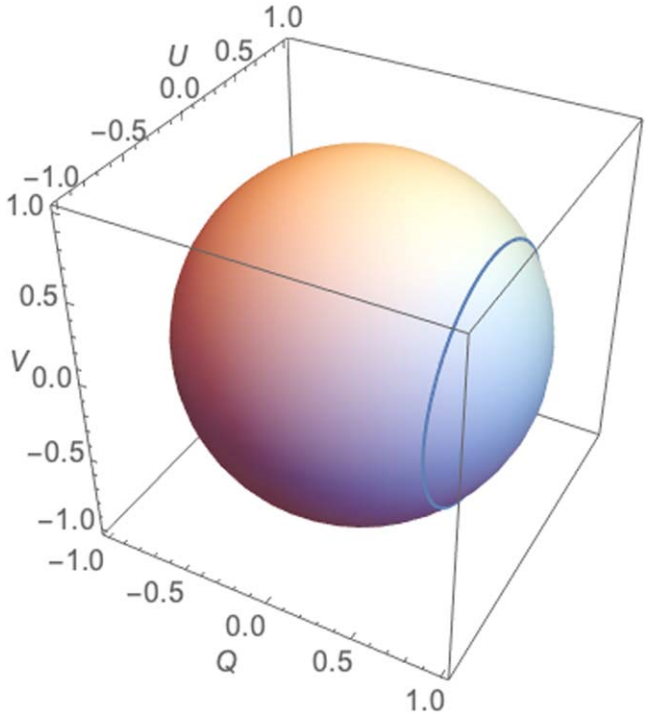

Figure 3. Example of the trajectory on the Poincare sphere for initial polarization in the $\chi_0 = \pi/8$ state ($Q = U = 1/\sqrt{2}$). The parameter Q remains constant.

Using Jones' calculus, at any location, the polarization can be characterized by a vector

$$\boldsymbol{E} = \begin{pmatrix} \cos\chi_0 \\ e^{i\delta}\sin\chi_0 \end{pmatrix} = \hat{J}\cdot\boldsymbol{E}_0$$
$$\hat{J} = \begin{pmatrix} 1 & 0 \\ 0 & e^{i\delta} \end{pmatrix}. \tag{10}$$

$\hat{J}$ is Jones' matrix.

The corresponding Stokes parameters (normalized to unity; a fully polarized wave is assumed) are

$$\hat{P} = \begin{pmatrix} Q \\ U \\ V \end{pmatrix} = \begin{pmatrix} \cos(2\chi_0) \\ \cos\delta\sin(2\chi_0) \\ \sin\delta\sin(2\chi_0) \end{pmatrix} = \begin{pmatrix} Q_0 \\ U_0\cos\delta \\ U_0\sin\delta \end{pmatrix} \tag{11}$$

The polarization transfer equation can be written as

$$\partial_z\hat{P} = \boldsymbol{\Omega}\times\hat{P}$$
$$\boldsymbol{\Omega} = (\partial_z\delta,\, 0,\, 0) \rightarrow \left(2\frac{\omega_p^2}{\omega c},\, 0,\, 0\right). \tag{12}$$

$\boldsymbol{\Omega}$ is the angular frequency of the polarization rotation rate on the Poincare sphere.

The corresponding Mueller matrix

$$\boldsymbol{M} = \begin{pmatrix} 1 & 0 & 0 & 0 \\ 0 & 1 & 0 & 0 \\ 0 & 0 & \cos\delta & -\sin\delta \\ 0 & 0 & \sin\delta & \cos\delta \end{pmatrix} \tag{13}$$

Thus, there are periodic $U-V$ oscillations (Figure 3). (It can be called ∼generalized Faraday conversion, but the proper Faraday effect—as opposed to the Cotton-Mouton effect—is not involved in this case).

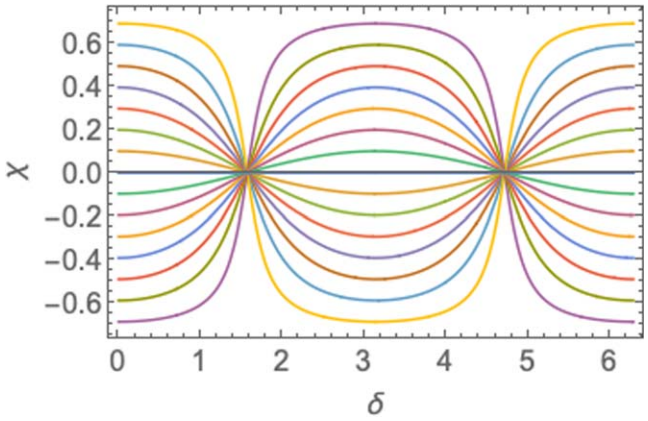

Figure 4. PA χ of linear polarization as a function of retardance δ for χ_0 between 0 and $\pi/2$ with a step $\pi/32$ ($\chi_0 = \pi/2$ is omitted—this would give a straight line at $\chi = \pi/2$). Values of $\chi = 0$ correspond to maximal circular polarization $V = U_0$ and $U = 0$.

The electric field traces an ellipse with ellipticity

$$\epsilon = \frac{\sqrt{\sqrt{1+\cos^2\delta\tan^2(2\chi_0)} - \cos^2\delta\sin(2\chi_0)\tan(2\chi_0) + \sin^2(\chi_0) - \cos^2(\chi_0)}}{\sqrt{\sqrt{1+\cos^2\delta\tan^2(2\chi_0)} + \cos^2\delta\sin(2\chi_0)\tan(2\chi_0) - \cos(2\chi_0)}} \tag{14}$$

and PA

$$\tan(2\chi) = \cos\delta\tan(2\chi_0); \tag{15}$$

see Figure 4.

Thus, in symmetric pair plasma, there is efficient transformation of Stokes parameters U and V, in a similar way to the laboratory phase retarders. The key parameter for the rate is the retardance δ, Equation (7). The rotation of polarization/production of the circular component in pair plasma disappears only for $U = 0$ with $2\chi_0 = 0,\ \pi$; this corresponds to either a pure X mode ($\chi_0 = 0$) or pure A-O mode ($\chi_0 = \pi/2$).

2.4. Frequency Scaling of the Generalized Faraday Rotation

In plasma, the retardance (Equation (7)) and rotation angle (Equation (15)) are wavelength dependent. The PA scales as

$$\partial_\lambda\chi = \frac{\sin(\delta)\tan(2\chi_0)}{2(1+\cos^2(\delta)\tan^2(2\chi_0))}\partial_\lambda\delta. \tag{16}$$

Equation (16) can be interpreted as a generalized Faraday rotation (GFR): frequency-dependent PA. Note that when the retardance crosses $\delta = \pi$ the sign of $\partial_\lambda\chi$, and the corresponding RM, changes (Dai et al. 2022)

At small $\delta \ll 1$ the frequency-dependent part of the PA scales as

$$\chi = \frac{\sin(4\chi_0)}{8}\left(\int\delta_0 dz\right)^2 \times \lambda^2. \tag{17}$$

Thus, frequency scaling matches the Faraday effect. But the polarization rotation in this limit is independent of the magnetic field (and hence cannot be used to estimate it). We can

introduce the effective RM, $\mathrm{RM_{eff}}$,

$$\begin{aligned}\chi &= \mathrm{RM}_{eff} \times \lambda^2\\ \mathrm{RM}_{eff} &= 10^{-4} \times \frac{\sin(4\chi_0)}{8}\left(\int \delta_0 dz\right)^2\\ &= 10^{-4} \times \sin(4\chi_0)\frac{e^4}{2m_e^2c^4}n^2(\Delta z)^2\\ &= 3 \times 10^{11} \times \sin(4\chi_0) \times \mathrm{DM}^2\,\mathrm{m}^{-2} \end{aligned} \tag{18}$$

(factor of 10^{-4} converts from cgs units to m^{-2}). Thus, to produce $\mathrm{RM} = 10^5$ in FRB 121102 (Michilli et al. 2018), the required DM is only 5×10^{-6}.

At special moments when $\delta \approx \pi/2$ we find from Equation (15)

$$\begin{aligned}\Delta\chi = \tan 2\chi_0 \Delta[\delta] &= \frac{e^2 nz \tan(2\chi_0)}{m_e c^2} \times \Delta[\lambda]\\ &= 8 \times 10^5 \tan(2\chi_0)\mathrm{DM} \times \Delta[\lambda]. \end{aligned} \tag{19}$$

At this point, the circular component is large. Note that in both cases $\delta \ll 1$ and $\delta \sim \pi/2$. the rotation angle is independent of the magnetic field. Generally, we can write

$$\begin{aligned}&\Delta\chi \propto \Delta[\lambda^p]\\ &1 < p < 2. \end{aligned} \tag{20}$$

In astrophysical literature, this is usually called generalized Faraday rotation.

In conclusion, we arrived at two important results: (i) There is the efficient production of a circular component in symmetric pair plasma; and (ii) the corresponding frequency scaling (in the $\delta \ll 1$ regime) matches the Faraday rotation. Thus, for the observed radio signal, if $\chi_{\mathrm{high}} - \chi_{\mathrm{low}}$, which is the rotation angle difference between the top and bottom frequencies, is much smaller than 1 rad, the generalized Faraday rotation may be confused with Faraday rotation and misinterpreted as a large RM or a sign change of the RM (although in the case of FRB 20190520B, the observed change in PA against frequency is large enough to distinguish different effects.)

In what follows, we apply the general relations derived above to relativistically streaming plasma in the inner parts of the pulsar/magnetar winds.

2.5. Faraday Conversion in Electron–Ion Plasma

All the above relations, when expressed in terms of retardance δ, Equation (6), are applicable to regular electron–ion plasma for propagation orthogonally to the magnetic field, when the normal modes are linearly polarized. In particular, a term similar to the $\omega_B \ll \omega$ limit in Equation (4) appears also in nonsymmetric plasma. In that case for wave propagating orthogonal to the magnetic field,

$$(\Delta n)_{e-i} = -\frac{\omega_B^2\omega_p^2}{2\omega^4} \tag{21}$$

The principles of Faraday conversion remain the same: In a frame defined in Figure 2, the Stokes Q remains constant while U and V experience oscillations. The rotation direction on the Poincare sphere $\mathbf{\Omega}$, Equation (12), is still aligned with Q.

In regular plasma at small ω_B, $\omega_p \ll \omega$, the retardance is (see Equations (21) and (6))

$$\frac{d\delta_{e-i}}{dz} = -\frac{\omega_B^2\omega_p^2}{2c\omega^3}. \tag{22}$$

It has a different sign and different frequency scaling from the $\omega_B \gg \omega$ case. The motion on the Poincare sphere in this case proceeds in the opposite sense around the Q-axis (counterclockwise instead of clockwise).

The sense of rotation on the Poincare sphere cannot be used to distinguish the two cases observationally: the Q–U separation is observer dependent (typically Q is chosen along the direction to the north). There is then a freedom in rotation on the Poincare sphere around the V-axis. Qualitatively, the difference between the phase speeds of the X mode and the A-O mode changes sign at the resonance, but observationally we do not know the direction of the magnetic field, hence we cannot define which mode is which: A change in the magnetic field direction by $\pi/2$ "flips" the observational definition of the X and A-O modes.

In constant density/magnetic field, the total retardance (Equation (22)) evaluates to

$$\delta_{e-i} = \frac{2\pi e^4}{m_e^3c^3\omega^3} \times \mathrm{DM} \times B^2 = 7 \times 10^{-3}\lambda^3 \mathrm{DM}\, B^2, \tag{23}$$

where DM is the dispersion measure in pc cm^{-3}, λ is in centimeters, and the magnetic field is in Gauss. The condition $\delta_{e-i} \sim 1$ is much more demanding than Equation (7).

3. Magnetar/Pulsar Winds

3.1. Particle Dynamics in the Inner Wind, $\mathrm{R}_{LC} \leqslant \mathrm{r} \leqslant \mathrm{r}_0$

Let us consider the motion of particles in the inner wind with a Michel (1973b) magnetic field and assuming that particles move exclusively along the field ("bead-on-wire" approximation). This is best done using the machinery of general relativity (Landau & Lifshitz 1975).

In spherical coordinates, changing to the rotating system of coordinates $d\phi \to d\phi' - \Omega dt$ and assuming that particles move along the Archimedean spiral with

$$d\phi' = -\Omega dr \tag{24}$$

at a fixed polar angle $d\theta_p = 0$, we find the metric tensor

$$\begin{aligned} g_{00} &= -(1 - r^2\sin^2\theta_p\Omega^2) = -g^{rr}\\ g_{rr} &= (1 + r^2\sin^2\theta_p\Omega^2) = -g^{00}\\ g_{rt} &= r^2\sin^2\theta_p\Omega^2 = g^{rt}. \end{aligned} \tag{25}$$

The Hamilton–Jacobi equation

$$g^{\alpha\beta}\partial_\alpha S\partial_\beta S = 1 \tag{26}$$

for the action functional S, with separation $S = -\gamma_0 t + S_r(r)$, becomes

$$\begin{aligned}&\gamma_0^2(r^2\Omega^2\sin^2\theta_p + 1) - 2\gamma_0 r^2\Omega^2\sin^2\theta_p S_r'(r)\\ &-S_r'(r)^2(1 - r^2\Omega^2\sin^2\theta_p) = 1. \end{aligned} \tag{27}$$

The Lorentz factor γ_0 comes mostly from the motion of particles along the magnetic field.

This can be integrated to find S_r. Differentiating the result with respect to γ_0, we find

$$t = r - \frac{1}{\sin\theta_p\Omega} + \ln\left(\left(1 - \frac{1}{\gamma_0^2}\right)\right.$$
$$\left.\times\frac{(1 - r\Omega\sin\theta_p)(\sqrt{\gamma_0^2 + r^2\Omega^2\sin^2\theta_p - 1} + \gamma_0 r\Omega\sin\theta_p)}{(1 + r\Omega\sin\theta_p)(\sqrt{\gamma_0^2 + r^2\Omega^2\sin^2\theta_p - 1} - \gamma_0 r\Omega\sin\theta_p)}\right)\frac{1}{2\sin\theta_p\Omega}. \quad (28)$$

Equation (28) gives the implicit solution for the motion of a bead along Michel-type magnetic field lines; time is chosen to be $t = 0$ at the moment when the particle crosses the light cylinder, $r = 1/(\sin\theta_p\Omega)$.

By differentiating with respect to time, we find the coordinate velocity

$$\beta_r \equiv \partial_t r = \frac{\varpi^2\Omega^2}{1 + \varpi^2\Omega^2}\times\left(1 - \frac{1}{\gamma_0^2 + \gamma_0^2\varpi^2\Omega^2 + \varpi^4\Omega^4}\right) + \frac{\gamma_0\sqrt{\gamma_0^2 + \varpi^2\Omega^2 - 1}}{\gamma_0^2 + \gamma_0^2\varpi^2\Omega^2 + \varpi^4\Omega^4}$$
$$\approx\begin{cases} 1 - \frac{1}{\gamma_0^2}, & \Omega\varpi \ll \gamma_0 \\ 1 - \frac{1}{\varpi^2\Omega^2}, & \text{for } \varpi \to \infty \end{cases}$$
$$\varpi = r\sin\theta_p. \quad (29)$$

The toroidal component of the velocity

$$v_\phi = \varpi(1 - \beta_r) \quad (30)$$

remains small; it is maximum value is reached at $\approx 1.27\ \gamma_0/\Omega$ and equals $v_{\phi,\max} \approx 0.3/\gamma_0$ (at $\theta_p = \pi/2$). Particles move nearly radially.

Relations (29)–(30) require some explanation. The motion of particles consists of (i) bulk E-cross-B drift and (ii) motion along the field. The bulk E-cross-B drift has two components, radial and toroidal (Michel 1973a):

$$\boldsymbol{v} = \left\{\frac{\varpi^2}{1 + \varpi^2}, 0, \frac{\varpi}{1 + \varpi^2}\right\}, \quad (31)$$

In the inner part of the wind the unit magnetic field vector

$$\mathbf{e}_B = \left\{\frac{1}{\sqrt{1 + \varpi^2}}, 0, -\frac{\varpi}{\sqrt{1 + \varpi^2}}\right\} \quad (32)$$

quickly becomes toroidal (the field lines intersect the light cylinder at 45°). As a result, near the light cylinder the large azimuthal drift velocity is mostly compensated by the azimuthal component of the parallel velocity, resulting in nearly radial motion with the relativistic Lorentz factor γ. Particles stream radially with Lorentz factor γ_0 (injection Lorentz factor). The EM waves propagate across magnetic field, $\theta = \pi/2$.

In conclusion, in the inner part of the wind, somewhat outside the light cylinder, particles move nearly radially with the Lorentz factor γ_0 determined by the acceleration processes inside the magnetosphere.

3.2. Wind Parameters

Let us parameterize the properties of the wind by the wind luminosity L_w and the ratio of the Poynting to particle fluxes μ:

$$\mu = \frac{L_w}{\dot{N}m_e c^2} = \frac{B_{\rm LC}^2}{4\pi n_{\rm LC} m_e c^2}$$
$$B_{\rm LC} = \frac{\sqrt{L_w}\Omega}{c^{3/2}}$$
$$n_{\rm LC} = \frac{L_w}{4\pi\mu m_e c^3 R_{\rm LC}^2}. \quad (33)$$

The terminal Lorentz factor of the wind is Γ_w; it is reached at r_w,

$$\Gamma_w = \mu^{1/3}$$
$$r_w = \mu^{1/3} R_{\rm LC} \quad (34)$$

(Michel 1969; Goldreich & Julian 1970; Michel 1973b). The requirement that $\Gamma_w \geqslant \gamma_0$ then gives $\mu \geqslant \gamma_0^3$. This is a requirement that the terminal Lorentz factor is determined by the wind acceleration, not by the injection.

If density is scaled to the Goldreich & Julian (1969) density $n = \kappa n_{GJ}$, then

$$\kappa\mu = \frac{e\sqrt{L_w}}{m_e c^{5/2}} = 3 \times 10^{10} L_{w,38}. \quad (35)$$

3.3. Cyclotron Resonance

One of the key issues is the location of the cyclotron resonance $\omega' \sim \omega'_B$. For a given frequency ω (in the observer frame), the cyclotron resonance occurs at

$$r_B = \frac{e\sqrt{L_w}}{c^{3/2} m_e \omega}$$
$$\frac{r_B}{R_{\rm LC}} = 30 L_{w,38}\nu_9^{-1}P^{-1}, \quad (36)$$

where period is in seconds. (Note that for the Crab pulsar, $P = 0.033$ s, the cyclotron resonance occurs at $\sim 10^3 R_{\rm LC}$.) Relation (36) is independent of the Lorentz factor of the wind.

3.4. Limiting Polarization Radius

The separation of modes into X and O branches may be violated if the rate of change of plasma parameters is sufficiently fast, so that the mode propagation becomes nonadiabatic (the effect of limiting polarization; Budden 1952). This occurs when the wavelength of the beat between two modes becomes larger than the scale at which the properties of the modes change. In our case, this condition becomes

$$\left(\frac{\omega}{\Gamma c}\right)\left(\frac{r}{\Gamma}\right)(\Delta n)' \geqslant 1, \quad (37)$$

where Γ is the Lorentz factor of the wind, which follows from Equation (29). This is a condition that propagation is adiabatic.

The condition for limiting polarization becomes

$$R_{\rm LP} = 2\frac{e^2}{m_e^2 c^4}\frac{L_w}{\Gamma\mu\omega} = \begin{cases} 2\frac{e^2}{m_e c^4}\frac{L_w}{\gamma_0\mu\omega}, & R_{\rm LP} \leqslant r_0 \\ \frac{\sqrt{2}e\sqrt{L_w}\sqrt{R_{\rm LC}}}{m_e c^2\sqrt{\mu}\sqrt{\omega}}, & R_{\rm LP} \geqslant r_0 \end{cases}. \quad (38)$$

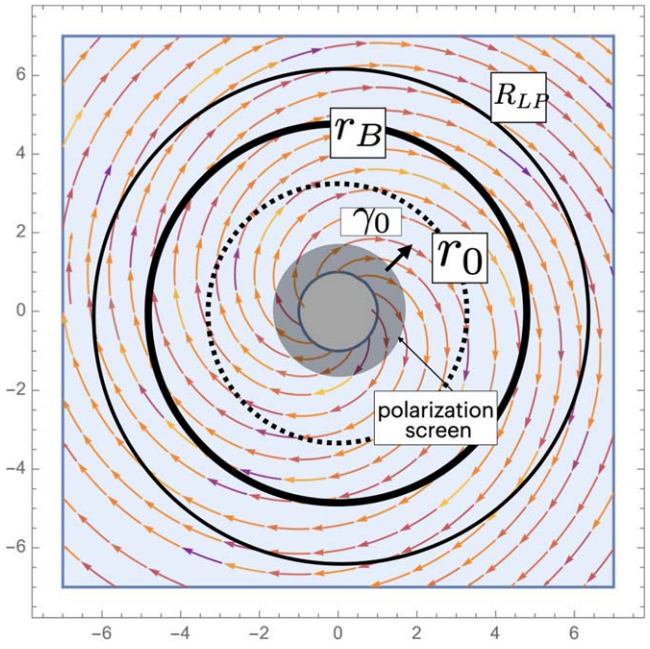

Figure 5. Geometry of PA rotation in the inner parts of the wind (not to scale). Arrows are the magnetic field (Michel 1973b). Particles leave the magnetosphere with Lorentz factor γ_0, moving nearly radially. At distance $r_0 \sim \gamma_0 R_{\rm LC}$, the Lorentz factor starts to increase $\gamma \propto r/R_{\rm LC}$. Cyclotron resonance occurs at r_B, and the limiting polarization radius is R_{LP}. Depending on the parameters of the flow, the relative locations of r_0, r_B, and R_{LP} may change.

The location of the limiting polarization radius is thus highly dependent on the parameter $\gamma_0\mu$. For definiteness, we assume $R_{\rm LP} \geqslant r_0$ (Figure 5).

4. Polarization Transfer in Magnetar Winds

4.1. Retardance and Generalized Rotation Measure in the Wind

Let us assume the following scaling in magnetar winds: $r_{\rm LC} \leqslant r_0 \leqslant R_{\rm LP}, r_w$ (see Figure 6), so that the cyclotron radius is outside the constant Lorentz factor region r_0. Let us consider polarization transformation in the regions $r < r_0 < r_B$, where $\omega_B \gg \omega$ and the Lorentz factor is constant $\sim \gamma_0$.

As we demonstrated in Section 3.1, the azimuthal motion of particles can be ignored. The wind can then be approximated as a sequence of toroidal magnetic loops moving away from the light cylinder. The EM waves propagate across a magnetic field, $\theta = \pi/2$, through a relativistically moving wind.

In this regime, the Lorentz factor of the particles is $\sim\gamma_0$, and $\omega \leqslant \omega_B$. The rate of retardance in the wind frame

$$\left(\frac{d\delta}{dt'}\right)' = \frac{\omega_p'^{,2}}{\omega'}. \tag{39}$$

Transformation to the lab frame gives

$$\frac{d\delta}{dt} = \frac{\omega_p^2}{\gamma_0\omega} \tag{40}$$

(values of ω_p^2 and ω transform similarly, while the rate is smaller in the observer frame.)

Estimating $\Delta z \sim R_{\rm LC}$ and the density according to Equation (33), we find

$$\delta \sim \frac{e^2}{2\pi m_e^2 c^6}\frac{L_w \Omega\lambda}{\mu\gamma_0} = 3.8 \times 10^{10}\,\frac{L_{sd,38}\lambda}{P\mu\gamma_0}. \tag{41}$$

The key dependence is on the combination of parameters $(\mu\gamma_0)$. It is very large, a product of two large numbers. For example, for the Crab pulsar with multiplicity $\kappa \sim 10^4$, this gives $\mu \sim 4\times 10^6$; for a typical $\gamma_0 \sim$ few $\times 10^3$, we find $\mu\gamma_0 \sim 10^{10}$.

To get a large phase shift $\delta \geqslant 1$ requires

$$\mu\gamma_0 \leqslant \frac{e^2}{2\pi m_e^2 c^6} L_w \Omega\lambda = 3.8 \times 10^{11}\, L_{w,38}\lambda P^{-1} \tag{42}$$

(period P in seconds).

The effective RM (Equation (18)) then becomes

$${\rm RM}_{eff} = 3 \times 10^{-7}\frac{\sin(4\chi_0)}{(\mu\gamma_0)^2}\frac{e^4}{m_e^4 c^{12}} L_w^2 \Omega^2 \tag{43}$$

(this assumes $\delta \leqslant 1$).

To produce an observed RM of value ${\rm RM}_{\rm ob}$, the ratio of the Poynting to particle fluxes and the streaming Lorentz factor should satisfy the condition

$$\mu\gamma_0 \leqslant 1.4 \times 10^8 \times \sqrt{\sin(4\chi_0)}\,\frac{L_{w,38}}{P\sqrt{{\rm RM}_{\rm ob}}} \tag{44}$$

(a smaller μ implies a larger observer frame density; a smaller γ_0 implies less time dilation).

In particular, for ${\rm RM}_{\rm ob} = 10^5$ inferred by Michilli et al. (2018), it is required that

$$\mu\gamma_0 \leqslant 5 \times 10^5 \times \sqrt{\sin(4\chi_0)} \times \frac{L_{w,38}}{P}. \tag{45}$$

Relations (41)–(43) are our main results. They provide estimates of the retardance and the RM through the inner part of the wind (expression for the ${\rm RM}_{\rm eff}$ assumes $\delta \leqslant 1$).

Models of pair creation in the pulsar magnetospheres (Ruderman & Sutherland 1975; Arons & Scharlemann 1979; Timokhin 2010) typically predict $\gamma_0 \sim 10^3$–10^5 and similarly for $\kappa \sim 10^3$–10^5. Thus, for the Crab pulsar, $\mu \sim 10^5$–10^7 and $\mu\gamma_0 \sim 10^9$–10^{11}; see Equation (35)). Such plasmas are too rarefied and too fast to produce an observable effect; see Equation (43).

Magnetar plasmas are expected to be much denser and slower. First, the basic current density can be much higher than the Goldreich–Julian density (Thompson et al. 2002). Second, the bulk Lorentz factor is expected to be smaller, $\gamma_0 \sim 10^2$ (Beloborodov 2013). For this value of the Lorentz factor, Equation (34) then implies that in order to satisfy Equation (45) the wind must be heavy loaded with $\mu \leqslant 10^3$; thus, $\mu \leqslant \gamma_0^3$ so that the terminal Lorentz factor of the wind is determined by the injection Lorentz factor γ_0, not the acceleration of the wind.

4.2. Polarization Evolution near the Cyclotron Resonance

The region near the cyclotron resonance r_B presents a challenge, both in terms of the possibility of cyclotron absorption, large rates of PA rotation, and harder to quantify effects of the Lorentz factor spread. If cyclotron absorption is negligible (Section 5) for a monoenergetic beam, a large

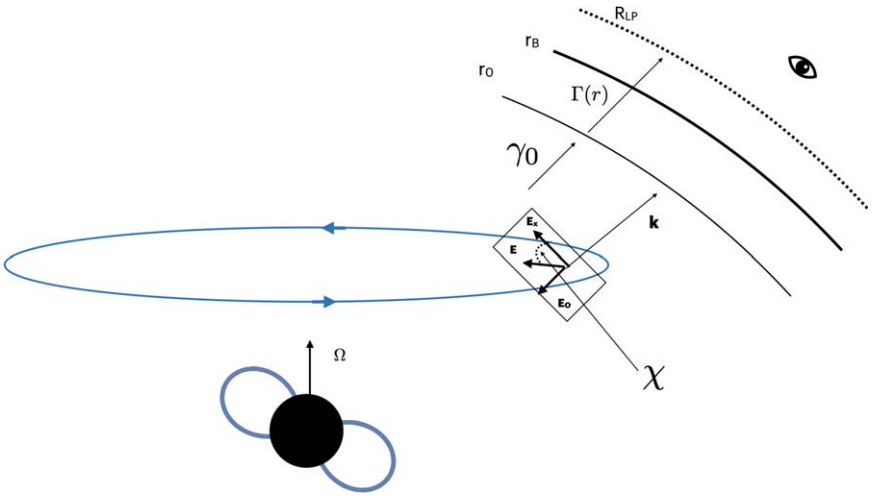

Figure 6. Particle dynamics and polarization in the inner wind. The magnetic field quickly becomes nearly toroidal, and particles stream nearly radially. Until $r \sim r_0 = \gamma_0$, the Lorentz factor is the injection Lorentz factor, determined by magnetospheric processes; at larger radii the wind accelerates linearly. Radiation produced in the magnetosphere can be separated into X and O modes. The linear component of polarization makes an angle χ with respect to the projection of the spin of the neutron star on the sky.

rotation angle near resonance will be mostly canceled, because at two sides of the resonance, the rotation direction is in the opposite sense. But a small mismatch between the inner and outer parts may produce a large net rotation near the resonance.

Near the cyclotron resonance the evolution of the retardance rate $d\delta/dz$ becomes infinitely fast (for a monoenergetic beam—to be smoothed out due to velocity spread). Most importantly, $d\delta/dz$ changes sign as the wave goes through the resonance. If the plasma density at both sides of the resonances were the same, then (in the absence of absorption) the total PA rotation angle would be zero. In the expanding wind, the plasma density "after" the resonance is smaller than "before." This creates a finite PA rotation as the EM pulse propagates through the resonance.

Integrating Equation (7) with Equation (4), we find for the resonant contribution

$$\delta|_{\rm res} \approx \frac{R_{\rm LC}\omega_{p,r_B}^2}{2c\omega}\ln\left(\frac{r_B}{R_{\rm LC}}\right) \approx \frac{R_{\rm LC}\omega}{4c\mu}\ln(r_B/R_{\rm LC}) \approx 5\times 10^3\mu_6^{-1}P\lambda^{-1}, \quad (46)$$

where ω_{p,r_B} is the plasma frequency at the resonance. Qualitatively, retardance (Equation (46)) resembles (7), with two modifications: (i) it is the density at the cyclotron resonance that appears in (46) (this reduces the rotation angle); (ii) the logarithm $\ln(r_B/R_{\rm LC}) \sim 10$ appears due to density imbalance at two sides of the resonance. Total PA rotation through resonance can be large.

Notice that retardance through the resonance is inversely proportional to wavelength: For longer waves, the location of the cyclotron resonance is proportional to λ, so that density at the resonance $\propto \lambda^{-2}$. This reduces the scaling $\delta \propto \lambda$ in constant density/magnetic field (Equation (7)) to $\delta \propto \lambda^{-1}$ in decreasing density/magnetic field.

5. Cyclotron Absorption in the Wind

5.1. General Relations

The resonant optical depth can be estimated as (Zheleznyakov 1996; Thompson et al. 1994; Lyutikov & Gavriil 2006)

$$\tau_{\rm res} \approx \sigma_{\rm res} n' \frac{r}{\Gamma}$$
$$\sigma_{\rm res} = \frac{\pi^2 e^2}{m_e c \omega_B'}$$
$$\tau_{\rm res} = \frac{e\sqrt{L_w}}{m_e c^{5/2}\mu\gamma_0} = 2\times 10^{10}\frac{L_{w,38}^{1/2}}{\mu\gamma_0}. \quad (47)$$

Given the limit on the product $(\mu\gamma_0)$ from above, Equation (45), the optical depth to cyclotron absorption is large.

In a strong magnetic field, a particle quickly emits a cyclotron-absorbed photon: In this case the process is resonant scattering, not absorption. The cyclotron emission time in the frame of the wind is

$$t_c' \approx \frac{m_e^3 c^5}{B'^2 e^4} \quad (48)$$

Comparing with flight time in the rest frame $(r/\gamma_0)/c$,

$$\frac{ct_c'}{r/\Gamma} = \frac{m_e^2 c^{11/2}\gamma_0^3}{e^3\sqrt{L_w}\omega} = 5\times 10^2\,\gamma_0^3 L_{w,38}^{-1/2} \gg 1. \quad (49)$$

Thus, it is absorption, not scattering.

Absorption will affect mostly the X mode (for propagation perpendicular to the magnetic field the A-O mode is not affected). Fluctuations of the wind density may still allow escape of the X mode and of the circularly polarized component.

5.2. Cyclotron Absorption in Crab Pulsar

Crab pulsar presents an interesting case: Using the fact that we do see emission from Crab, we can constrain the magnetospheric Lorentz factor γ_0. Detection of Crab pulses at the highest frequencies of $\sim$50 GHz imposes constraints on the properties of particles accelerating in the magnetosphere and on the wind properties.

Observations of the Crab Nebula require $\kappa \geqslant 10^5$ for high-energy emission (Hibschman & Arons 2001; Luo et al. 2020), and even more for radio (Shklovskii 1977; Atoyan 1999). Models of pulsar high-energy emission arising due to inverse Compton scattering (Lyutikov et al. 2012; Lyutikov 2013) also require high multiplicities $\kappa \geqslant 10^6$, though in that case it is the local/instantaneous multiplicities, while the estimates for the Crab Nebula infer average multiplicity.

Single pulses from Crab have been seen at $\sim$50 GHz (Hankins et al. 2016). Transparency at these frequencies impose the toughest constraints, as we discuss next.

If expressed in terms of the surface fields and the spin (known for Crab), the cyclotron resonance occurs at

$$\frac{r_{\rm res}}{R_{\rm LC}} = 2\frac{B_{\rm NS}R_{\rm NS}^3\Omega^3}{m_e c^4 \omega} = 5 \times 10^3 \nu_9^{-1}. \quad (50)$$

So, 100 MHz should be absorbed at 5×10^4 light cylinder radii, while 50 GHz should be absorbed at $\sim$100. (Condition $\omega' \leqslant \omega'_B$ also implies that induced scattering in the wind; Wilson & Rees 1978; Sincell & Krolik 1992, is suppressed at $r \leqslant r_{\rm res}$)

Using Equations (35) and (47), the resonant optical depth is

$$\tau_{\rm res} = \frac{\pi}{8}\frac{\kappa}{\Gamma}$$
$$\Gamma = \max[\gamma_0, r_B/R_{\rm LC}]. \quad (51)$$

Thus, to see pulses at 50 GHz, where γ_0 is likely $\geqslant r_B/R_{\rm LC} \sim 100$, it is required that $\gamma_0 \geqslant \kappa$: parallel Lorentz factor within the magnetosphere should be larger than the multiplicity parameter of the Goldreich & Julian (1969) density. It is a hard one to satisfy—most likely the nonstationarity of the flow plays a role.

5.3. Rotational Phase Evolution of Stokes Parameters

Above we assume a given direction of linear polarization produced in the magnetosphere and calculate the evolution of the polarization vector on the Poincare sphere. The tracks on the Poincare sphere we compute are for a single given EM signal with a given polarization, as a function of the retardance —local plasma parameters times the propagation distance. The observed temporal evolution of the PA is then a convolution of a possibly phase-dependent emitted PA (e.g.,, given by the rotating vector model, RVM), and the propagation effects.

For example, using RVM (Radhakrishnan & Cooke 1969) to produce χ_0 in Equation (15),

$$\tan\chi_0 = \frac{\sin\alpha\sin\phi}{\sin\alpha\cos\phi\cos\theta_{\rm ob} - \cos\alpha\sin\theta_{\rm ob}}. \quad (52)$$

We can plot the evolution of $\{Q, U, V\}$ as functions of the retardance and rotational phase ϕ, Figures 7–8. For fixed retardance (left panel in Figure 8), tracks on the Poincare sphere may be used to determine the absolute position of the projection of the axis of rotation on the plane of the sky—Q should remain fixed.

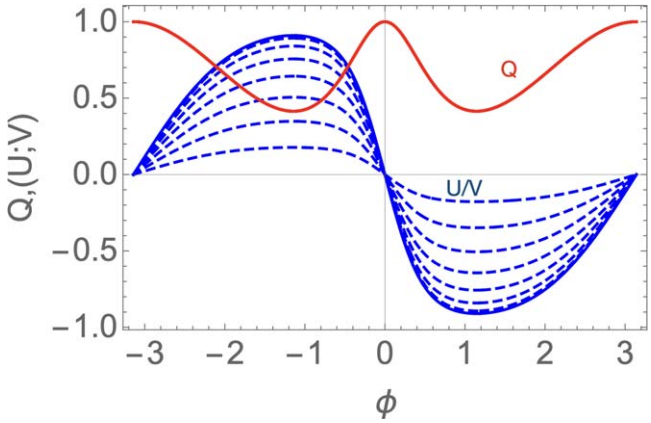

Figure 7. Evolution of Stokes parameters as a function of rotational phase ϕ and different retardance for $\alpha = \pi/8$, $\theta_{\rm ob} = \pi/4$ assuming that the initial phase is given by the rotating vector model. Solid lines correspond to zero retardance (for $V = 0$). Dashed lines are for U–V tracks in retardance steps of $\pi/16$. U and V curves match each other with a shift of retardance of $\pi/2$ (modulo the sign).

We stress that RVM may not be applicable to magnetar/FRB radio emission (and to Crab pulsar). RVM assumes that the global dipole structure of field lines determines the local polarization properties of the emitted radiation. In magnetars and FRBs, the structure is expected to be highly nondipolar and solar like (Lyutikov 2002, 2015, 2021). Another complication may come from the fact that for oblique rotators, the plasma density along the line of sight (and hence the retardance at each moment) may be phase dependent.

6. Discussion

We discuss the properties of polarization transfer in the near wind regions of magnetars, presumed loci of FRBs; the magnetospheric model of radio emission from magnetars and FRBs (Lyutikov 2002; Popov & Postnov 2013; Lyutikov & Popov 2020; Lyutikov 2021) is assumed. We point out the importance of wave propagation in the inner parts of the magnetar's winds. Qualitatively, a phase shift between the X and O components of the order of a wavelength, $\sim$centimeters, leads to large changes in the polarization properties.

The birefringent pair-symmetric plasma works as a wave retarder, periodically converting Stokes U into Stokes V (in a properly defined frame, where one of the axes is aligned with the magnetic field). Unlike the case of conventional Faraday conversion, here Q–U oscillates in phase (because the Q–U separation depends on the coordinate frame chosen).

The model offers explanations for (i) the large circular polarization component observed in FRBs, with right–left switching; (ii) large RM, with possible sign changes (if the observed PA change against frequency is less than 1 rad in the observed frequency range); and (iii) time-dependent variable polarization. A relatively dense and slow wind is needed—the corresponding effect in regular pulsars is small.

The present model offers a way to produce a large circular polarization and large RM, both with changing signs in FRB 20190520B (Dai et al. 2022). Relatively dense plasma is required—in regular pulsars, this effect is less important than in magnetars (which are expected to produce denser winds). Pulsars clearly do not show such wild polarization behavior. The rotating vector model (Radhakrishnan & Cooke 1969),

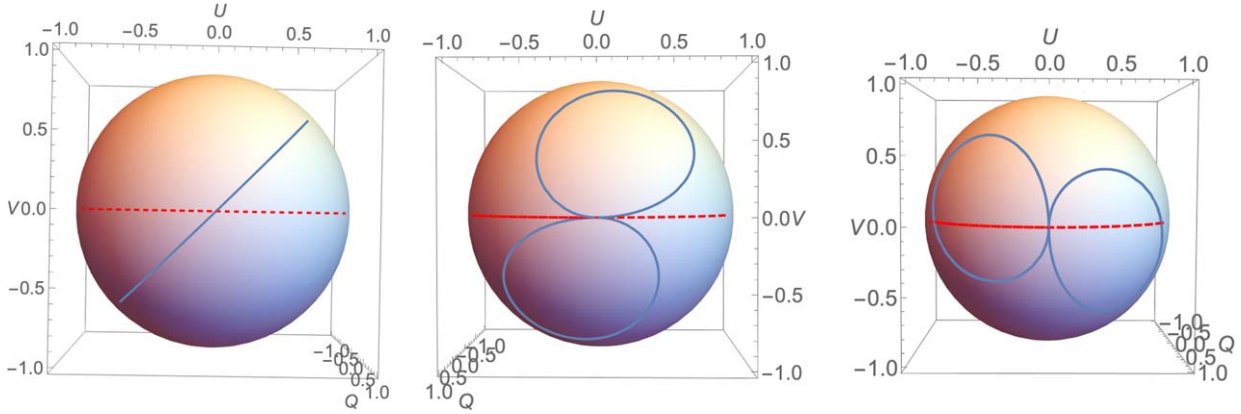

Figure 8. Combined effects of RVM and propagation. Pictured are examples of trajectory on the Poincare sphere for different scalings of the retardance with the phase (e.g., due to density variations along the line of sight). In case of no propagation effects, the RVM predicts that the trajectory is a big circle $V = 0$ (dashed red). Left panel: fixed retardance $\delta = \pi/4$ (tilted big circle). Center panel: $\delta = |\phi|$. Right panel: $\delta = \pi/2 + |\phi|$. More complicated dependence of the retardance on the phase would result in correspondingly more complicated trajectories on the Poincare sphere.

which neglects all the propagation effects, does account for many pulsar PA profiles (though there are many exceptions when it is not; e.g., in Crab). Relation (43) gives the simplest estimate of the PA effect in the wind. The propagation effects are not important in regular pulsars, with a low plasma density and high γ_0 (the Goldreich & Julian 1969 density is much smaller than what is expected in magnetars; Thompson et al. 2002; Beloborodov & Thompson 2007).

The main prediction of the model is that scaling of the PA with frequency may deviate from the conventional RM with $\chi \propto \lambda^2$. The reverse is not true: The model does allow for $\chi \propto \lambda^2$ scaling, especially at small retardance $\delta \ll 1$. There are observational hints; the most interesting analysis is by Price et al. (2019), their Figure 8. They demonstrate that a linear relation $\chi \propto \lambda$ is consistent with data.

Most observational works typically assume a regular RM scaling: In fact, the frequency behavior of polarized components must be fitted independently (e.g., Kumar et al. 2022).

If the system of coordinates is aligned with the projection of the spin axis on the plane of the sky, then during propagation via a symmetric pair wind, Stokes Q remains constant while U and V experience periodic oscillations. The separation between Q and U depends on the chosen system of coordinates, $\times$ versus $+$. Because the expected track on the Poincare sphere involves only U–V oscillations, this could be used to determine (to 90° uncertainty) the projection of the pulsar/magnetar spin on the plane of the sky. For example, a constant position on the Poincare sphere with $V = 0$ may imply that this is a pure Stokes Q (an alternative explanation would be that propagation effects are not important while the emitted PA is constant.)

Finally, magnetars show variations in activity on timescales from days to months (Kaspi & Beloborodov 2017). It is expected that winds are similarly variable. Variations in the density of the wind will lead to medium-to-long timescale variations of the polarization properties.

This work had been supported by NASA grants 80NSSC17K0757 and 80NSSC20K0910, and NSF grants 1903332 and 1908590. I would like to thank Vasily Beskin, Andrei Gruzinov, Marcus Lower, Yuri Levin, Yuri Lyubarski, Kiyoshi Masui, Donald Melrose, Alexandre Philippov, Eric Poisson, and Louise Willingale for discussions.

The data underlying this article will be shared on reasonable request to the corresponding author.

ORCID iDs

Maxim Lyutikov https://orcid.org/0000-0001-6436-8304

References

Arons, J., & Barnard, J. J. 1986, ApJ, 302, 120
Arons, J., & Scharlemann, E. T. 1979, ApJ, 231, 854
Atoyan, A. M. 1999, A&A, 346, L49
Barnard, J. J. 1986, ApJ, 303, 280
Beloborodov, A. M. 2013, ApJ, 777, 114
Beloborodov, A. M., & Thompson, C. 2007, ApJ, 657, 967
Beskin, V. S., & Philippov, A. A. 2012, MNRAS, 425, 814
Born, M., & Wolf, E. 1980, Principles of Optics Electromagnetic Theory of Propagation, Interference and Diffraction of Light (Oxford: Pergamon)
Budden, K. G. 1952, RSPSA, 215, 215
Caleb, M., van Straten, W., Keane, E. F., et al. 2019, MNRAS, 487, 1191
Cheng, A. F., & Ruderman, M. A. 1979, ApJ, 229, 348
Dai, S., Feng, Y., Yang, Y. P., et al. 2022, arXiv:2203.08151
Ginzburg, V. L., & Syrovatskii, S. I. 1965, ARA&A, 3, 297
Goldreich, P., & Julian, W. H. 1969, ApJ, 157, 869
Goldreich, P., & Julian, W. H. 1970, ApJ, 160, 971
Gruzinov, A., & Levin, Y. 2019, ApJ, 876, 74
Hankins, T. H., Eilek, J. A., & Jones, G. 2016, ApJ, 833, 47
Hibschman, J. A., & Arons, J. 2001, ApJ, 560, 871
Kaspi, V. M., & Beloborodov, A. M. 2017, ARA&A, 55, 261
Kazbegi, A. Z., Machabeli, G. Z., & Melikidze, G. I. 1991a, MNRAS, 253, 377
Kazbegi, A. Z., Machabeli, G. Z., Melikidze, G. I., & Smirnova, T. V. 1991b, Ap, 34, 234
Kennett, M., & Melrose, D. 1998, PASA, 15, 211
Kumar, P., Shannon, R. M., Lower, M. E., Deller, A. T., & Prochaska, J. X. 2022, arXiv:2204.10816
Landau, L. D., & Lifshitz, E. M. 1960, Electrodynamics of Continuous Media (Energy Conversion Management) (Oxford: Pergamon)
Landau, L. D., & Lifshitz, E. M. 1975, The Classical Theory of Fields (Oxford: Pergamon)
Luo, Y., Lyutikov, M., Temim, T., & Comisso, L. 2020, ApJ, 896, 147
Lyutikov, M. 1999, JPlPh, 62, 65
Lyutikov, M. 2002, ApJL, 580, L65
Lyutikov, M. 2007, MNRAS, 381, 1190
Lyutikov, M. 2013, MNRAS, 431, 2580
Lyutikov, M. 2015, MNRAS, 447, 1407
Lyutikov, M. 2021, ApJ, 922, 166
Lyutikov, M., & Gavriil, F. P. 2006, MNRAS, 368, 690
Lyutikov, M., Otte, N., & McCann, A. 2012, ApJ, 754, 33
Lyutikov, M., & Popov, S. 2020, arXiv:2005.05093
Masui, K., Lin, H.-H., Sievers, J., et al. 2015, Natur, 528, 523
Melrose, D. B. 1997, PhRvE, 56, 3527
Michel, F. C. 1969, ApJ, 158, 727

Michel, F. C. 1973a, ApJ, 180, 207
Michel, F. C. 1973b, ApJL, 180, L133
Michilli, D., Seymour, A., Hessels, J. W. T., et al. 2018, Natur, 553, 182
Petroff, E., Hessels, J. W. T., & Lorimer, D. R. 2019, A&ARv, 27, 4
Petrova, S. A., & Lyubarskii, Y. E. 2000, A&A, 355, 1168
Popov, S. B., & Postnov, K. A. 2013, arXiv:1307.4924
Price, D. C., Foster, G., Geyer, M., et al. 2019, MNRAS, 486, 3636
Radhakrishnan, V., & Cooke, D. J. 1969, ApL, 3, 225
Ravi, V., Shannon, R. M., Bailes, M., et al. 2016, Sci, 354, 1249
Ruderman, M. A., & Sutherland, P. G. 1975, ApJ, 196, 51
Sazonov, V. N. 1969, SvA, 13, 396
Shklovskii, I. S. 1977, SvA, 21, 371
Sincell, M. W., & Krolik, J. H. 1992, ApJ, 395, 553
Thompson, C., Blandford, R. D., Evans, C. R., & Phinney, E. S. 1994, ApJ, 422, 304
Thompson, C., Lyutikov, M., & Kulkarni, S. R. 2002, ApJ, 574, 332
Timokhin, A. N. 2010, MNRAS, 408, 2092
Vedantham, H. K., & Ravi, V. 2019, MNRAS, 485, L78
Wang, C., Lai, D., & Han, J. 2010, MNRAS, 403, 569
Wilson, D. B., & Rees, M. J. 1978, MNRAS, 185, 297
Zheleznyakov, V. V. 1996, Radiation in Astrophysical Plasmas, Vol. 204 (Berlin: Springer)